PAPER • **OPEN ACCESS**

Integrating control and sensing in SMA-based actuators for shape-morphing hinge structures

To cite this article: Carmen Ballester *et al* 2026 *Smart Mater. Struct.* **35** 025002

Smart Materials and Structures

OPEN ACCESS

RECEIVED
11 November 2025

REVISED
26 December 2025

ACCEPTED FOR PUBLICATION
20 January 2026

PUBLISHED
2 February 2026

PAPER

Integrating control and sensing in SMA-based actuators for shape-morphing hinge structures

Carmen Ballester[1,*], **Kaspar Jansen**[2], **Dorin Copaci**[1] and **Sepideh Ghodrat**[2]

[1] RoboticsLab, Department of Systems Engineering and Automation, University Carlos III of Madrid, Avda. Universidad, 30, Leganés 28911, Madrid, Spain

[2] Emerging Materials Laboratory, Department of Sustainable Design Engineering, Faculty of Industrial Design Engineering, Delft University of Technology (TU Delft), Landbergstraat 15, Delft 2628 CE, The Netherlands

[*] Author to whom any correspondence should be addressed.

E-mail: cballest@ing.uc3m.es

Keywords: shape memory alloy actuators, position control, shape-morphing structures

Abstract

Shape memory alloys (SMAs) offer unique advantages for compact, high-force actuators in shape-morphing systems, yet current solutions rarely provide modular torsional actuation with integrated closed-loop control and embedded sensing. Here, we present a novel modular hinge system featuring a compact, feedback-controlled torsional SMA actuator and miniaturized Hall effect sensing, designed for scalable and reconfigurable adaptive and shape-morphing structures. Our system enables real-time trajectory tracking with robust movement range and actuation time response achieving mean tracking errors below 1° and passive recovery above 40% in sinusoidal tests. By detailing actuator-sensor integration, proportional-integral-derivative control architecture, and wireless communication protocols, we demonstrate the advantages of modularity for constructing multi-degree-of-freedom assemblies. These results establish a versatile platform for high-performance, adaptive, and interactive shape-morphing technologies, advancing the field of smart materials for robotics and intelligent structures as a whole.

1. Introduction

Smart materials are defined as materials that have the ability to change their physical or chemical properties autonomously in response to an external stimulus, such as temperature or light. These materials provide a powerful tool for new design paradigms, because they can perform both sensing and actuation functions, and so, they are inherently interactive materials [1]. Shape memory alloys (SMAs) are one of the most used smart materials to develop actuators, because they can exert very high forces relative to their weight, making them a highly energy-dense material. SMAs are a class of metallic materials that can recover a predetermined shape after being deformed, when exposed to appropriate temperature changes or mechanical loading. This property arises from a reversible, solid-state phase transformation between two key phases: austenite, with a symmetrical structure that occurs at higher temperature than martensite; and martensite, which occurs at lower temperature and is easily deformed [2].

The shape memory effect (SME) describes the ability of an SMA to 'remember' and return to its original shape upon heating, while superelasticity (SE) refers to the alloy's capacity to sustain large, reversible strains at temperatures above the austenite finish temperature, due to stress-induced phase transformation and immediate recovery upon unloading. These unique properties form the basis for a wide range of SMA applications in engineering and smart systems [3]. These actuators are often applied to engineering because they are also flexible and lightweight, such as robotics [4], automotive and aerospace [5] and medical applications [6]; but SMAs are not limited to engineering and can also be found applied to other fields like fashion, art, architecture and spatial design [1].

SMA-based actuators are typically available in wire or coil forms and generate linear displacement when heated [7]. However, recent approaches are exploring new possibilities of deformation by changing the initial form of the commercial SMA to a specific shape, training the material in a ceramic oven.

In particular, torsional deformation is being studied because SMA actuators are one of the most compact possible approaches to achieve rotational movement under load, even though they have limitations such as high power requirements and low actuation frequencies [8]. Some works are applying thin SMA sheets to achieve torsion, such as in [9] and [10], while others are studying the feasibility of developing miniaturized torsion SMA-based actuators for future applications, such as aircraft actuation [11], self-deploying structures [12] or biomedical tools for surgical procedures [13].

In general, all the systems with integrated actuators can be classified as either non-controlled or controlled. Non-controlled systems, also referred to as 'open-loop' in control theory, are characterized by a lack of knowledge about the actuator's current state. In SMA actuators this translates to a constant heating of the material, independent of the current temperature, resulting in two states: only heating and only cooling. This approach is suitable for simple tasks where the intermediate states of the SMA are not required, and it is often applied to bistable devices such as deployable structures [14] or structural beams [15]. Other works use SMA-based actuators in an open-loop system for more complex tasks, but control the movement of the system through design and morphology, for example, [16] uses SMAs to power a bio-inspired swimming jellyfish.

Nevertheless, for more advanced movements that require different actuation velocities, movement amplitudes, or trajectory following, a controlled approach is necessary for SMA-based actuators. When controlled, the current state of the material is known, and heating depends on the difference between the current state and the desired state, which can range from fully heated to fully cooled. The ability to respond differently to different environmental changes using the same actuator increases the range of applications for SMA-based actuators and enables more accurate movement when interacting with the surroundings. The most used controller in literature for SMA-based actuators is a proportional-integral-derivative (PID) controller, because it offers a simple yet robust solution for reference following. This controller is applied in a variety of different applications, as in [17], where it is used to control the position of a ball on a rotary beam; or in [18], where SMAs move a soft tentacle fitted with a camera for deep-sea exploration. Other approaches use the PID controller as a base and then explore more complex control schemes to overcome the material non-linearities, such as robust control for a multi-wire soft manipulator [19]; or adaptive control to improve the actuators response in human-robot interactions [20].

Developing a controlled system with SMA-based actuators increases its complexity, as it requires the integration of a sensor to measure the state of the material, which is usually inferred using temperature and/or position measurements. Temperature can be measured inside the system using thermocouples, such as in [21], offering an small and easy-to-integrate sensing solution. Another option is to use external thermal readings with infrared cameras, as in [22] and [23], as these are often more precise. Although temperature sensors provide accurate information about the internal state of the SMA, they are usually too slow or complex to be integrated into a miniaturized system for real-time control and are usually used for modeling the material's behavior. On the other hand, position sensors offer a reliable off-the-shelf solution for tracking the deformation of SMA-based actuators, thanks to their compact size, which makes the integration into the system design very straightforward. More precisely, Hall effect position sensors are very popular because they offer a contactless solution that only requires a magnet to provide precise readings of the actuator's position. These sensors can be found with controlled SMA-based actuators in several compact devices, for example to control the movement of a snake robot [24] or to develop a reconfigurable robotic end-effector [25].

From a design perspective, SMA-based actuators can be categorized as shape-morphing devices, which are defined as structures that can change their shape to support dynamic affordances, enhance human or robotic dexterity and customize physical interfaces [26]. These new structures are studied and applied in various fields, including energy optimization in buildings [27] and engineering applications such as soft robotics and deployable space structures [28]. Although SMAs are often used in shape-morphing structures due to their properties [29], most of the works apply them in an open-loop strategy, such as in [30] and [31]. Other works, such as [32], focus on the modularity of the design, to provide a higher insight and possibilities to scale the design. By changing the paradigm and adding control to the system, the structure will be able to respond to different environmental conditions using the same actuator, significantly increasing the potential applications for shape-changing devices. For example, a starfish robot was developed in [33] and a spatially stable structure for robotics is proposed in [34], using linear and spring SMA actuators, respectively.

However, there have been no significant breakthroughs in literature regarding the integration of controlled SMA torsion actuators into modular, shape-changing structures. Researching the control of SMA torsion actuators, which have a higher energy density than axial SMA actuators, would enhance the development of scalable, adaptable modular shape-morphing structures. This would constitute an

improvement in the tools available for the design of all types of interactive devices and structures, which would be a significant advancement in the field.

In this work, we present the integration of an accurate position-controlled, torsional SMA-based actuator into a modular hinge that can be used as a fundamental building block for reconfigurable, shape-morphing structures. The developed hinge can follow different trajectories and achieve different actuation times and target angles, according to the generated target trajectory. The structure of this paper is organized as follows: section 2 details the developed hinge components, both the mechanical and the electronic system; section 3 explains the different validation and performance tests; section 4 covers the analysis of the main results and their implications and finally section 5 contains the main conclusions of this work.

2. Methods

2.1. Mechanical design

2.1.1. Actuator

The actuator selected to produce the movement is based on a reversible hinge actuator previously developed [35]. In this work, two Nitinol wires were combined: one working with SME and the other with SE. The main concept is that, once heated, the SME recovers its original shape and deforms the SE. Then, when the heating stops, the SE wire acts as a spring and applies external force to the SME to deform it again.

To ensure the wires work in opposite directions, considering that for the recovery phase a passive SE wire is selected, they must be pre-trained in a ceramic oven at a specific initial angle. Figure 1(a) shows the initial angle, θ_0, for each wire. In this case, the SME wire is trained to 0°, so when heated, it closes the hinge. The SE wire is trained to π rad, so it will open the hinge and deform the SME wire. The result of training the wires in the ceramic oven is two Nitinol wires, as shown in figure 1(b). These wires can be easily integrated into a variety of designs. The working principle of the actuator is depicted in figure 1(c). First, when cold, the actuator is open and the SME wire is deformed to π rad. Upon heating, the SME wire recovers its trained position, closing the hinge until it reaches θ_H and deforming the SE wire. Finally, when the heating stops and the SME wire begins to cool down, the SE wire returns to its original position, θ_C, deforming the SME wire again and opening the hinge to complete the cycle.

In order to accurately dimension the actuator, it is necessary to define the torque that the wires can exert so the actuator can be designed to respond to any application constraints. By dimensioning the torque, it is possible to know the forces that the actuator can generate and thus, the payload that can move. According to the classical mechanics definition, the torque τ of each wire can be express as in equation (1), where G is the shear modulus of the material, J is the polar moment of inertia, which for the wire is defined in equation (2), L_T is the torsion length and D is the diameter of the wire. The torque is proportional to the deformation angle, wire diameter, shear modulus, and polar moment of inertia, and inversely proportional to the torsion length. These parameters must be selected carefully to ensure that the actuator's forces comply with the application constraints,

$$\tau(\theta) = \frac{GJ}{L_T}\theta \tag{1}$$

$$J = \frac{\pi D^4}{32}. \tag{2}$$

Before selecting the final actuator configuration, different SME-SE combinations were assembled and tested as preliminary results. To analyze the behavior of the actuator, an SME wire is selected according to commercial availability and combined with different SE wires. The torque generated by the SME cable must be sufficient to deform the SE cable and overcome the inertia and friction of the physical components of the hinge, and the torque generated by the SE cable must be sufficient to recover the initial position of the SME. Table 1 details all mechanical parameters, as well as the calculated polar moment of inertia and torque for the SME cable and four different SE cables. These torque values are consistent with the previous analytical study of the torque produced by the hinge actuator considering different angles and temperatures, detailed in [35].

Sample 2 of SE, with a diameter of 0.5 mm, generates very low torque compared to the torque generated by the SME, so the actuator does not recover at all. Sample 3 of SE has a diameter of 1 mm, so it generates such high torque that the SME cable cannot initiate movement because it is not able to deform the SE cable and overcome the dynamics of the physical system. Finally, Sample 4 with a 0.83 mm SE generates an intermediate torque that produces a bidirectional movement: the SME cable can deform and then the SE can recover the initial position of the SME to a certain extent. The training angle also

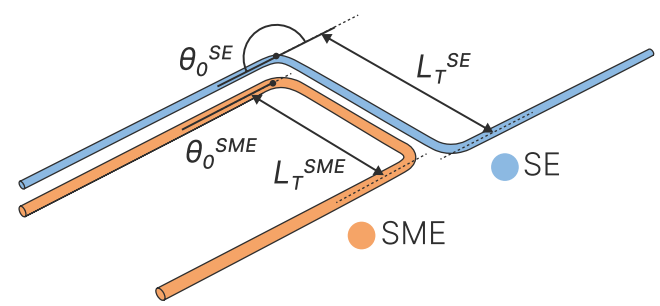

(a) SME and SE pre-trained shape scheme.

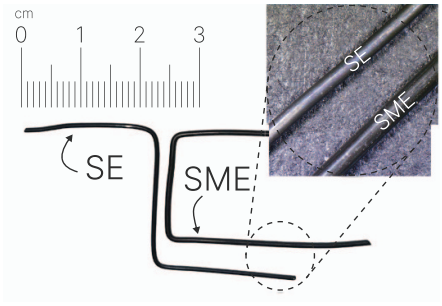

(b) SME and SE wires photograph.

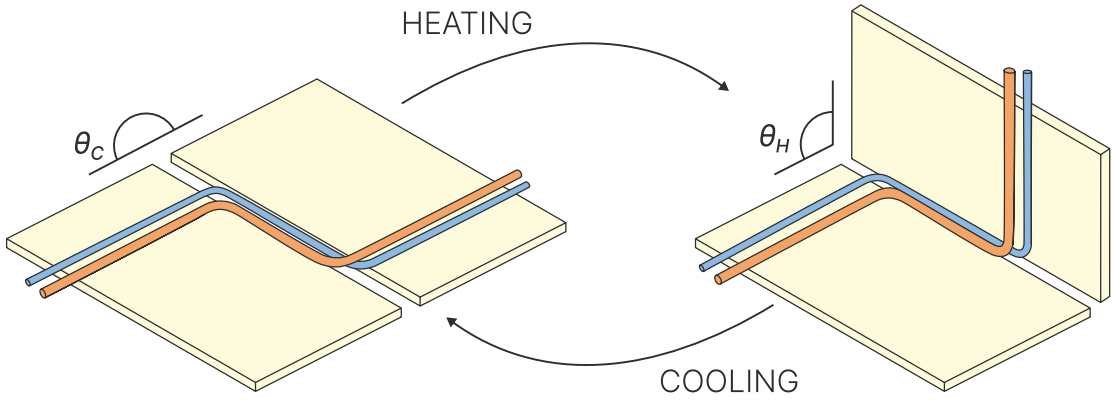

(c) Nitinol-based torsional actuator movement scheme.

Figure 1. Nitinol-based torsional actuator design with a pre-trained initial angle in the ceramic oven. The actuator is a combination of a SME wire that actuates upon heating and a SE wire that actuates upon cooling, resulting in a hinge movement.

Table 1. SME and SE wire's mechanical properties: diameter (D), torsion length (L_T), polar moment of inertia (J) (2), shear modulus (G) [35], trained angle (θ_0) and torque ($\tau(\Delta\theta)$) (1).

	Sample	D[mm]	L_T[mm]	J[mm^4]	G[GPa]	θ_0[rad]	$\tau(\Delta\theta)$[Nm]
1	SME [36]	1.0	15.4	0.098	25.4 (A) 14.7 (M)	0	0.1619 0.0937
2	SE [37]	0.5	22.7	0.006	23.4	π	0.0063
3	SE [37]	1.0	21.5	0.098	23.4	π	0.1069
4	SE [38]	0.83	23.2	0.047	23.4	π	0.0470
5	SE [38]	0.83	20.9	0.047	23.4	$-\pi/2$	0.0522

Table 2. SME and SE wire's chemical compositions and critical phase transformation temperatures [35].

	Sample	Ni–Ti[%]	M_s[°C]	M_f[°C]	A_s[°C]	A_f[°C)]
1	SME	55.6–44.4	16.6	−2.5	30.2	37.8
4	SE	55.0–45.0	0.5	−44.8	−18.5	12.5

influences the torque generated, since depending on the initial angle, the deformation in the heating state is greater or lesser. Sample 5 of the SE shows a training angle of $-\pi/2$, so that when the actuator is at rest in the initial state, the SE already has a deformation of $\pi/2$. This configuration allows the recovery force to be increased, as the recovery force increases as the deformation increases. However, this initial deformation substantially reduces the maximum angle of movement of the actuator, given that the SME requires more force to deform the SE during heating. The final actuator is assembled using the 1 SME and the 4 SE wires, as this is the only configuration that provides a bidirectional movement. Table 2 shows the chemical composition of the selected Nitinol wires and a thermal characterization made by differential scanning calorimetry [35].

2.1.2. Sensor

Measuring the hinge movement is a crucial step in achieving control of the hinge movement, as it provides precise feedback about the current state of the actuator transformation. Due to the size of the

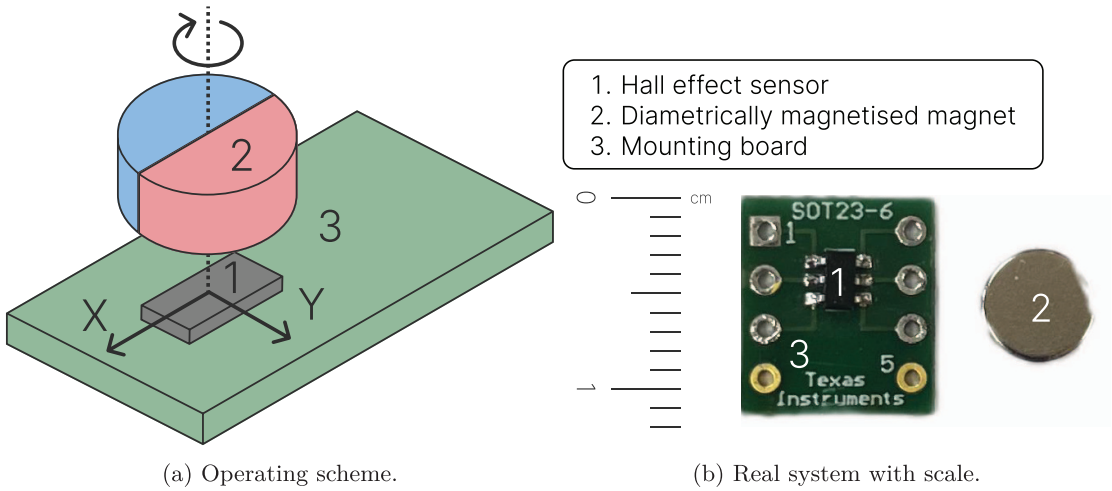

(a) Operating scheme. (b) Real system with scale.

Figure 2. Hall effect sensor used for angle measurements. When the diametrically magnetized neodymium magnet rotates over the sensor, the magnetic field changes, and the sensor converts that change into an absolute angle measurement,

actuator, the angle sensor must be as compact as possible, easy to integrate and contactless to minimize friction losses. For this study, the chosen sensor is the TLE Hall effect angle sensor, produced by Infineon ([39]), which offers precise angle readings in a miniaturized, contactless 3D design. The Hall effect is defined as the apparition of a voltage across the sides of a semiconductor plate when a current flows through this semiconductor in the presence of a magnetic field perpendicular to the current.

Infineon's TLE sensors integrate three orthogonally oriented plates, so they can sense the three magnetic field vector components B_x, B_y and B_z. Under a magnetic field $\vec{B}$, the Hall plate of the X-axis senses the projection of $\vec{B}$ onto its direction B_x, and so on for B_y and B_z. The rotation of a magnet around the sensor changes the components of the magnetic field vector sinuisodally, so from these magnetic field measurements the rotation angle θ is obtained according to equation (3). The magnet must change the magnetic field when rotating in the desired plane, so it is noted that it must be diametrically magnetized to change B_x and B_y, as shown in figure 2(a)

$$\left\{\begin{matrix} B_x = \vec{B}\cdot\cos\theta \\ B_y = \vec{B}\cdot\sin\theta \end{matrix}\right\} \longrightarrow \theta = \arctan\left(\frac{B_y}{B_x}\right). \tag{3}$$

The commercial sensitivity of the sensor, S_B, is 65 μT/LSB for each magnetic component B_i, $i \in (x, y, z)$, meaning that the digital output will change one bit each 65 μT. The magnetic field is then converted into a digital output using equation (4),

$$\Delta B_i = S_B \cdot \Delta \mathrm{LSB}_i. \tag{4}$$

The sensor's angle sensitivity is defined as the differential angle $\mathrm{d}\theta$, that is calculated using the chain rule in the previous equation (3), obtaining the following equation (5),

$$\mathrm{d}\theta = \frac{\delta\theta}{\delta B_x}\mathrm{d}B_x + \frac{\delta\theta}{\delta B_y}\mathrm{d}B_y = \left(-\frac{B_y}{B_x^2+B_y^2}, \frac{B_x}{B_x^2+B_y^2}\right)\cdot\left(\mathrm{d}B_x, \mathrm{d}B_y\right). \tag{5}$$

Considering a 1-LSB change in each axis, i.e. $\Delta B = S_B$, and using the norm of the gradient vectors, the previous formula can be easily approximated by assuming $\mathrm{d}\vec{B} \approx \Delta B$. The following equation (6) determines the sensor sensitivity for angle readings, which depends on the magnetic field reading for each axis. As the magnetic field depends on the strength of the magnet and the distance to the sensor, the angle sensitivity is application-dependent and cannot be generalized,

$$\Delta\theta \approx \|\nabla\theta\| \cdot \Delta B = \frac{\Delta B}{\sqrt{B_x^2+B_y^2}}. \tag{6}$$

The sensor is manufactured in a highly compact PG-TSOP6-6-8 package with dimensions of 2.9 mm $\times$ 1.6 mm, making it suitable for integration into a variety of systems, as shown in figure 2(b). It can be mounted on a custom-designed PCB or a commercially available board for wiring purposes.

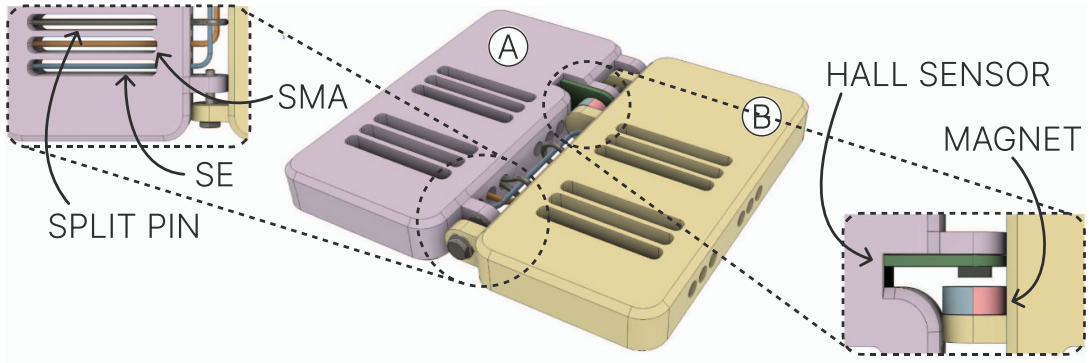

(a) Single hinge integration details.

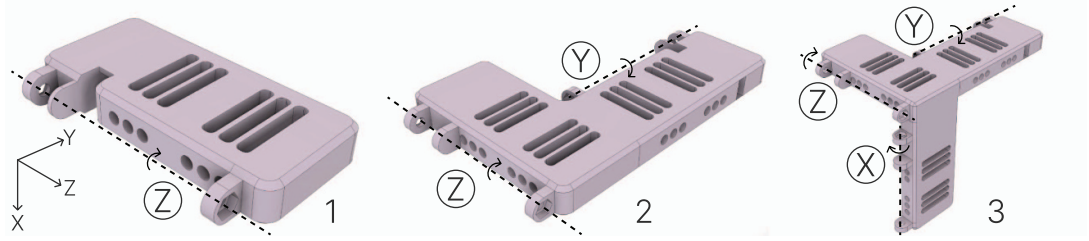

(b) Different panel shapes for allowing rotation over different axes and more complex movements.

Figure 3. 3D model of the integration of the actuator and sensor into a torsion structure composed by two rotating plates. The plates can be modified to add more rotation axes and achieve more complex rotations when combined with each other.

The sensor provides a 12-bit digital output for each magnetic field component. Communication with the microcontroller is achieved via the I2C protocol, which requires two pull-up resistors between the power supply and the I2C lines in the instrumentation circuit.

2.1.3. Design

A hinge consists of two connected plates that rotate relative to one another. To keep the system compact and maximize the possible opening and closing angles, the magnet and sensors were not mounted onto the panels, but integrated inside the panel halves (see figure 3(a)). The panel halves were 3D printed and contain eyelets for joining and spaces for split pins for guiding the actuator wires. To actuate the system, one leverage arm of the SME-SE wires is fixed to one plate, and the other leverage arm is fixed to the opposing plate, so when the actuator is heated the hinge closes and opens correspondingly. As the SME wire is thermally actuated, the plate design incorporates cut-outs around the actuators to enhance airflow, thereby accelerating cooling.

For sensor integration, it is necessary to align the centers of rotation of both the magnet and the Hall sensor. To achieve this, the two plates are fastened together with screws and bolts, ensuring proper alignment of the rotational axis during hinge motion. As the magnet and Hall sensor must rotate relative to each other, the magnet is required to be embedded in one plate and the sensor in the other. Accordingly, each hinge is formed from two complementary plates, A and B. Plate A contains the Hall sensor and includes a support to attach the sensor to minimize the sensor-magnet distance and thereby increase sensitivity. It also features a channel for routing and protecting the wiring within the hinge. Plate B supports the magnet, providing a platform for fixation.

The mechanical design allows proper alignment of the sensor and the actuator to produce controlled rotational movement. Additionally, the connection of the SME wire to the power supply is done through end-sleeves, and all the sensor wiring is inserted into the design, resulting in a small, lightweight and clean structure with seamless integration where the actuator and the sensor are barely noticeable.

A single hinge is therefore composed of two A and B plates. However, one plate can also host multiple hinges. The number of hinges per plate defines its degrees of freedom (DoF), so different plate designs and DoF configurations can be combined across various rotational axes, as illustrated in figure 3(b). This modular approach enables the design of multiple plate types that can be assembled into customizable kinematic structures, adaptable to the requirements of different devices and tasks. Based on the previous examples, table 3 summarizes the properties of each plate and establishes a nomenclature for their use in modular chains. Each DoF is identified by the axis of rotation and the plate model, and this convention applies consistently across all DoFs within a plate.

Table 3. Proposed multi-degree of freedom modular plates' parameters and modularity nomenclature for combination into shape-morphing structures.

Plate	Weight (g)	Size X–Y–Z (mm)	Number of DoF	Rotation	Model	Name
1	5.88	$8 \times 30 \times 54$	1	Z	A	L1-ZA
2	11.72	$8 \times 84 \times 54$	2	Z Y	B A	L2-ZB-YA
3	17.41	$62 \times 84 \times 54$	3	Z Y X	B A B	L3-YB-ZA-XB

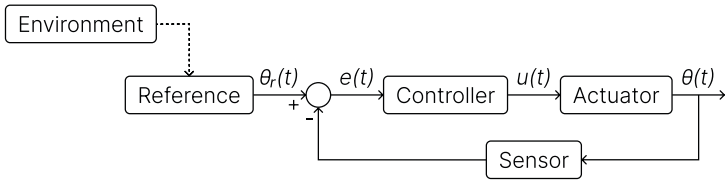

Figure 4. Closed-loop control scheme for trajectory following. The target trajectory can be generated according to the environment, and then the controller receives the difference between the desired and the current actuator angular position to heat the SME.

In general, increasing the number of DoFs enlarges the plate dimensions and, consequently, its weight. For prototyping purposes, the plates were fabricated from PLA with a 15% infill density. However, material selection must be carefully considered in future implementations to balance the weight of the plates against the torque output of the actuator, for example using thermoplastics like Polyetheretherketone.

Increasing the number of DoF increases the mechanical and electronic complexity of the system. For each independent movement of the joint, a low-level controller is needed to ensure trajectory following, and then there must be a high-level controller to plan the independent trajectories of each plate, ensuring smooth movements and avoiding auto-collisions within the structure. For this reason, the selected controller must remain simple, robust and fast in order to be scalable for multi-DoF systems in real-time.

2.2. Control and electronics

The mechanical design successfully integrates the actuator and the sensor that measures the angle of the hinge, providing feedback about its state and allowing a control scheme to be implemented in the system. Figure 4 illustrates the most common control closed-loop, where the actuator position $\theta(t)$ is regulated to follow a desired reference angle $\theta_r(t)$. Then, the controller computes the error $e(t)$ as the difference between the reference and the actual angle. Based on this error, the controller generates a control signal, $u(t)$, which is applied to the actuator to induce motion. This closed-loop configuration enables the hinge to adapt dynamically to environmental changes, since the reference angle can be updated in real time.

For SMA-based actuators, the control signal corresponds to the duty cycle of a pulse width modulation (PWM) signal. This PWM signal is generated by the microcontroller and then amplified by a power electronics stage to heat the SME wire via the Joule effect. In this work, a PID controller is employed because its robustness and simplicity. Equation (7) presents the control law governing the PID controller in continuous time domain, which then has to be discretized when implemented in the microcontroller. Table 4 lists the controller gains, which were empirically tuned for this application by a trial-and-error process,

$$u(t) = K_p e(t) + K_i \int_0^t e(t)\,dt + K_d \frac{de(t)}{dt}. \tag{7}$$

The main control loop is executed on a microcontroller, and to ensure efficient data management, a client-server communication protocol based on user datagram protocol (UDP) is implemented. Figure 5 depicts the architecture of this protocol. The client, which in this case is a Raspberry Pi 4B, executes the control loop, including sensor acquisition, error computation, and actuator command generation.

Table 4. PID controller parameters, selected empirically for this specific task.

K_p	K_i	K_d
5.0	2.0	0.5

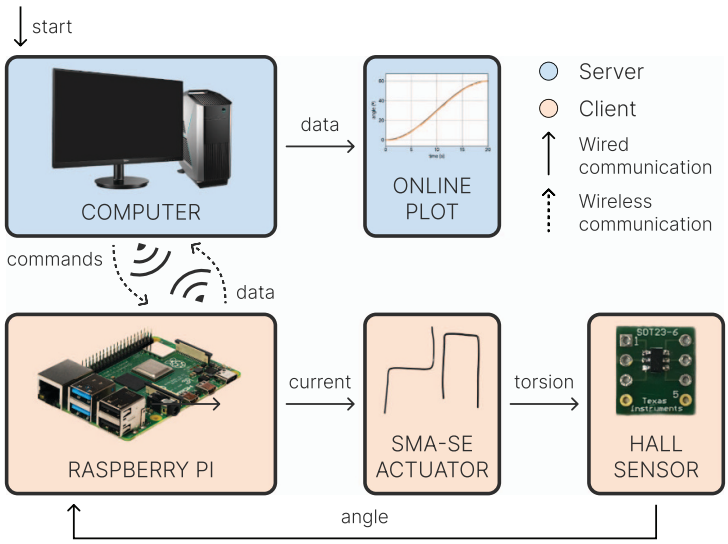

Figure 5. Wireless communication system using user datagram protocol (UDP) with Server–Client architecture. This approach maintains the control loop in the microcontroller but more computationally expensive tasks, like data visualization and management, are sent to the server and do not interfere with the main execution.

The server, which can be any type of computer, manages process supervision by sending start and stop commands to the client, thereby initiating or terminating the control loop. Furthermore, the server displays in real time all the process data transmitted by the client, such as actuator angle and control signal. Finally, the data is stored at the end of each execution to ensure proper data management. By separating the data management from the process using a wireless communication protocol, the small electronics is mounted into the device, thereby enhancing the integration of the hinges into real-world applications.

3. Results

The validation of the developed hinge as a shape-morphing structure is achieved by the independent evaluation of the integration and the performance of the actuator. These two different analyses provide precise information about the properties of each system's component, allowing for a better understanding of the limitations to improve in future works. One of the main limitations is that the actuator presents asymmetric activation, as only the heating of the SME wire can be actively controlled. Meanwhile, the mechanical deformation to return to the initial angle depends on the cooling of the environment and the passive force exerted by the SE wire.

To consider this asymmetry, the tests consist of two parts. In the heating phase, the SME wire follows a predefined trajectory, and then, the hinge's recovery capacity is studied, considering the effect of the SE wire force in the system. In the heating, the target trajectory, $\theta_r(t)$, follows a sinusoidal signal that is defined by a maximum value (the angle setpoint, θ_{max}) and the time to reach this setpoint (the actuation time, T_a), according to equation (8), where ϕ and θ_{of} are the temporal and angle offsets, respectively. For the cooling part, it is simply a step signal that returns to the initial angle until the test is completed. As the cooling of the actuator influences its recovery, and in order to standardize testing, the room temperature is set to 25 °C, and air convection currents are avoided,

$$\theta_r(t) = \theta_{max} \cdot \sin\left(\frac{4\pi}{T_a}t + \phi\right) + \theta_{of}. \tag{8}$$

3.1. Modular shape-morphing structures

The first integrated hinge, depicted in figure 6, has only 1 DoF to validate the integration of the components and their proper operation. Figure 6(a) shows the hinge during the test when it is following the reference: initial angle, maximum angle, and recovered angle. The heating of the SME wire is achieved

(a) Pictures of the integrated system in different states of the test.

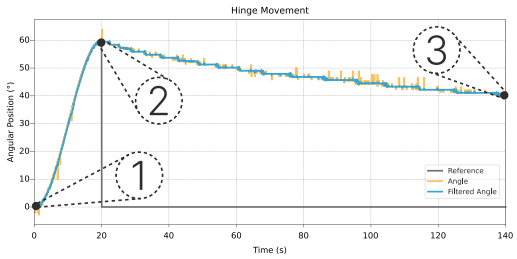

(b) Angular position over time.

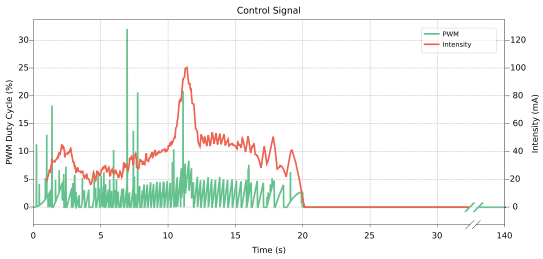

(c) Generated control signal during heating.

Figure 6. Hinge response for an angle setpoint of 60° and 20 s actuation time. The hinge closes up to the maximum reference value, following the trajectory shape because of the controlled heat, and then it is left to cool down for 2 min to recover its original angular position.

through Joule's Effect, using a PWM signal with 2 A of amplitude and 500 Hz of frequency, working at 10 V.

The followed trajectory is plotted in figure 6(b), where the custom target trajectory and the reading from the Hall effect sensor can be seen. The sensor reading is filtered to reduce the noise to improve readability using a uniform 1D filter. Overall, the hinge follows the reference in the heating without any problem, meaning the control signal is able to regulate the amount of current supplied to the wire for it to close at a certain rate. The computed control signal by the PID controller, shown in figure 6(c), maintains a value of around 5% of duty cycle, which translates to approximately 50 mA of current per second considering the PWM parameters. The higher marginal values of the PWM signal correspond to noise in the sensor readings produced by magnetic interference between the Hall effect sensor and the rotating magnet. When the SME reaches the maximum angle value the controller shuts down the power automatically to avoid over-heating the wire. Then, for the cooling part, when the target trajectory drops to 0, the SME wire starts cooling down and then the SE wire starts deforming back the SME wire to its initial position in the hinge.

The position graph in figure 6(b) shows one of the main limitations of the actuator, that is, the passive recovery using the SE wire. There are two main characteristics of the recovery curve: the rate and the percent of angle recovery. In this case, the recovery rate of the curve is very low because of the thermal actuation. The percent of recovered angle is influenced by the temperature and the force exerted by the SE, which have to be balanced in order for the hinge to open in the first place. In general, SMAs used in passive recovery scenarios, like this one, always present the problem of partial recovery because of the complexity of the force balance. To address this issue, the training angles could be adjusted to extend below 0° and above 180°.

Thanks to the simplicity of the actuator, it is possible to develop modular structures, maintaining the energy requirements. By using the proposed design in section 2.1, different modular shape-morphing structures can be developed by increasing the sensor and actuation integration to incorporate as many DoF as needed in one plate. When scaling the system, the number of DoF must be studied in terms of energy consumption, as the Joule effect heating of the actuator requires high currents that can easily increase the required power and constrain the application. The wire diameter selection is crucial, as smaller diameters need less current but they produce lower forces, so the wire selection must be optimized according to the task constraints. In addition, defining which joint movements are independent and implementing the low-level controllers and the high-level controller also can increase the system complexity and the computational power required to process all the data in real-time.

Figure 7 shows two different modular structures developed to validate the integration design, highlighting the versatility to modify the plates according to the desired task. The first proposed configuration, depicted in figure 7(a), represents a kinematic chain with 5 DoF, meaning that it can generate 5 independent movements to rotate the 6 plates between them. This configuration is very common, for

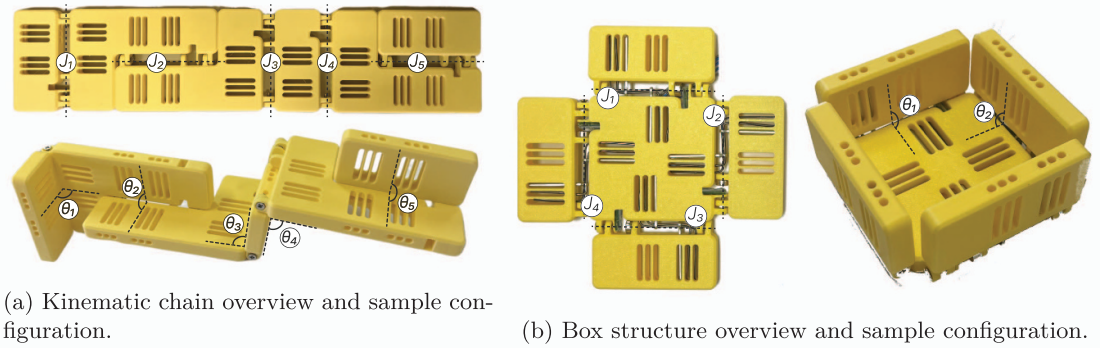

(a) Kinematic chain overview and sample configuration.

(b) Box structure overview and sample configuration.

Figure 7. Examples of modular shape-morphing systems created by the combination of different hinges with different rotation axes. The first example is a kinematic chain, where the plates follow a sequence, and the second example is a box-like structure that can have coordinated activation.

example, in robotics applications, where the tip of the system needs to move in a 3D space. The second configuration is represented in figure 7(b), and in this case the main idea is to form a box-like structure that can close and open. It consists of one main plate, the base, with 4 DoF, and then one single hinge for each side. In this configuration, it is possible to choose between either having independent opening and closing of each side, or activate all the hinges at the same time, using the sensors to ensure that all the hinges reached the desired position.

The main advantage of this controlled scheme is that the target trajectory can change when the system's environment changes. Using the previous configurations, and for example having the level of light in the environment as a variable, it is possible that the chain configuration follows the light by adjusting each hinge target trajectory, and that the box opens or closes depending on the amount of light in the environment.

3.2. Actuator performance

The actuator's performance is evaluated through the study of the trajectory following in the heating phase and the passive recovery of the position in the cooling phase. A trajectory is defined in robotics as the complete time-dependent sequence of positions, meaning that it is composed by the geometric route of the actuator and the times and motion dynamics for following that path. Studying the performance of the actuator for trajectory following allows the analysis of its suitability for applications in fields where the movement is constrained by predefined trajectories. For the heating phase, the main parameters that can impact in the trajectory are the movement range and the velocity of the movement. The study of the actuator's response to the variation of these parameters allows a comprehensive information about the constraints of the actuator. For the actuator's cooling phase is studied the percent of recovered angle, as it adds information about how the heating can affect the recovery of the initial position.

The first thing to study are the mechanical constraints, which in this case is the maximum angle. If the setpoint angle exceeds the maximum attainable angle of the hinge system the controller will keep heating the wire, and can increase the wire temperature over its specifications and lead to loss of actuation power. For this reason, the maximum and minimum angle values are the first thing that should be studied, considering that they depend on wire length, diameter, activation temperatures, etc. figure 8 shows the angle setpoint test, where the reference trajectories and the sensor readings are plotted over time. To evaluate the hinge's maximum reachable angle, the amplitude of the sinusoidal trajectory signal is increased from 20° to 80°. When the angle setpoint is 20°, depicted in figure 8(a), the actuator reaches the maximum angle, but the behavior of the trajectory is not smooth, presenting an oscillating trajectory. This response is very common for SMA-based actuators, because they are a thermal system that accumulates heat and has high inertia, so the system overshoot around the reference value, producing the oscillations. This effect is mitigated when the velocity increases, as shown in figures 8(b) and (c). For these tests, the hinge reaches the angle setpoint and the trajectories are smoother, because the increase in velocity reduces the accumulated heat in the system. Finally, figure 8(d), shows that the actuator does not reach the maximum value, only reaches 60° and it maintains that angular position, creating a mechanical plateau in the graph.

Once the maximum actuation range is defined, it is possible to evaluate the effect of the actuation time of the signal in achieving said angle. Figure 9 illustrates the performed tests, where the angle setpoint is constant at 60° and the actuation time increases. Just as the last figure, the graphics show the

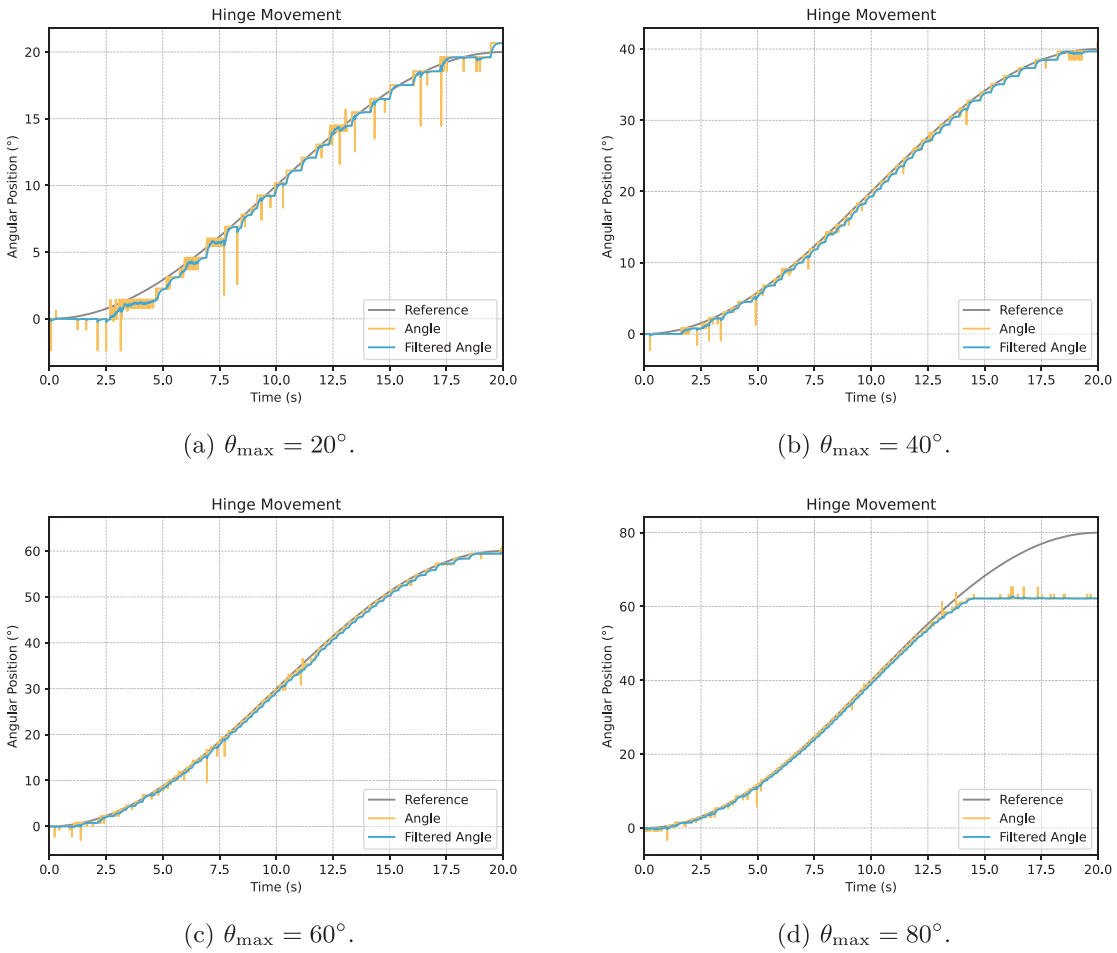

(a) $\theta_{\max} = 20°$. (b) $\theta_{\max} = 40°$.

(c) $\theta_{\max} = 60°$. (d) $\theta_{\max} = 80°$.

Figure 8. Actuator's angular position over time for different angle setpoints during 20 s of actuation time, to analyze the maximum closing angle.

reference trajectory and current angle measurements over time. For higher actuation times, of $T_a = 20$ s and $T_a = 10$ s, depicted respectively in figures 9(a) and (b), the actuator reaches the maximum angle within the time limits, following the trajectory smoothly. However, for lower actuation times of $T_a = 6.7$ s and $T_a = 5$ s, shown in figures 9(c) and (d) respectively, the actuator cannot follow the reference trajectory in the maximum values of the signal. Another noticeable error in these signals is the error at the start of the test, where the actuator needs to overcome the inertia to start the movement, and with higher velocities this gap is more visible.

For the cooling phase, the performance is studied through the analysis of the recovered actuator's angle for different actuation times and angle setpoints. The twelve conducted tests are defined by the combination of the angle setpoints $\theta_{\max} = 20, 40, 60°$ with the actuation times $T_a = 20$, 10, 6.67, 5 s. The recovery results are represented in figure 10, where the obtained values are represented by angle-frequency heatmaps to easily determine the worst and best performances, marked in blue and yellow respectively. For this work, the recovered angle is defined as the difference between the actuator's maximum and final position value and the frequency is defined as $f = 1/(2 * T_a)$.

Figure 10(a) depicts the percentage recovery; that is, the ratio of the angle recovered during passive cooling to the maximum angle reached during actuation, for each setpoint and actuation frequency. This is a normalized metric that reveals the relative efficiency under different conditions. The best efficiency scenario, which is higher frequencies for lower angles, reaches a percentage recovery of 46.91%. In addition, as the frequency increases, the heating is quicker, meaning that the accumulated heat in the system is reduced, and thus the recovery is improved. The worst case, only 33.75% of recovery, is for the combination of lower frequencies and higher angles, where the actuation time is higher and the system accumulates more heat.

However, to study the range of movement, the percentage of recovery is not as important as the absolute angle recovered in degrees, which is the direct difference between the maximum reached value and the final recovered position after cooling. Figure 10(b) shows that the lower angle setpoints only

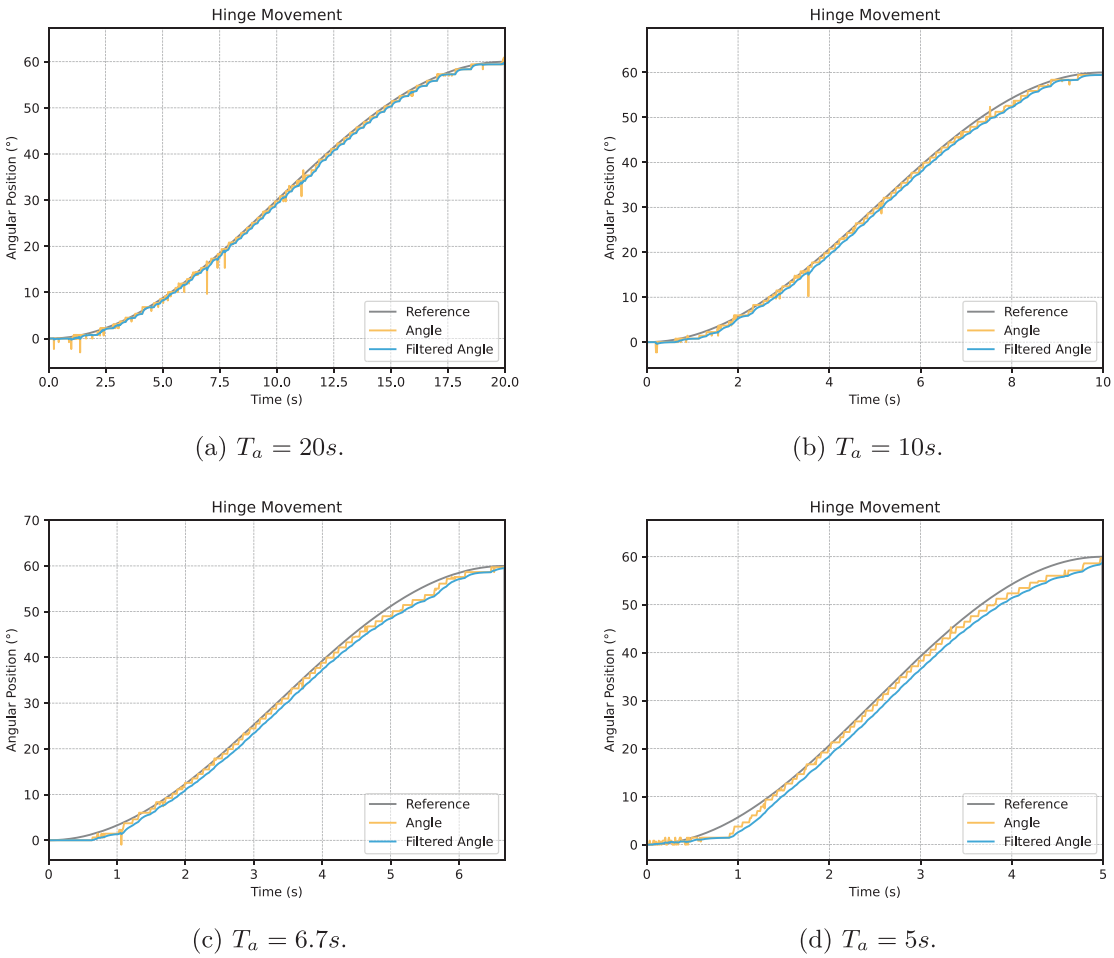

(a) $T_a = 20s$. (b) $T_a = 10s$.

(c) $T_a = 6.7s$. (d) $T_a = 5s$.

Figure 9. Actuator's angular position over time for different actuation times at 60° angle setpoint, to analyze the maximum closing velocity.

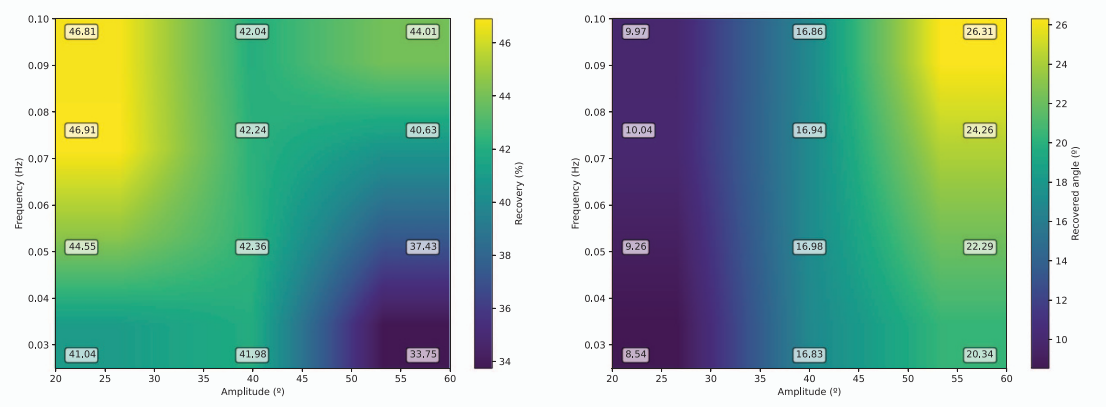

(a) Percentage of recovery for relative efficiency assessment. (b) Absolute angle recovered for movement range assessment.

Figure 10. Actuator's recovery values for all 12 tests, considering the unique frequency ($f = 1/(2 * T_a)$) and angle setpoint combination for each test, in a heat-map visualization format where higher recovery values are presented in lighter colors. The recovery is defined by the percentage of total angle recovered (a) and then as the recovered angle in degrees (b).

reach a maximum of 10.04°, as the overall movement is very limited. In addition, the frequency's impact for the higher angle setpoint is very noticeable, the lowest actuation time yields the best angle recovery for all tests, reaching a movement of 26.31°.

In terms of actuator performance, the movement is very limited in the recovery phase. The first involved factor is the thermal nature of the SMAs, which requires extra time to cool down before

Table 5. Mean and standard deviation values for the mean root square error (MRSE), mean applied current and the percentage of recovery grouped by both actuation time and angle setpoint, to evaluate the impact of the target trajectory in the performance and study the repeatability of the tests.

		Heating		Cooling
		MRSE (°)	current (mA s^{-1})	recovery (%)
Actuation time (s)	20	0.81 ± 0.19	33.1 ± 4.53	38.92 ± 3.68
	10	0.83 ± 0.07	39.6 ± 17.5	41.44 ± 2.98
	6.7	0.91 ± 0.13	55.2 ± 27.0	43.26 ± 2.66
	5	1.04 ± 0.29	71.1 ± 36.1	44.28 ± 1.96
Angle setpoint (°)	20	0.92 ± 0.06	28.7 ± 7.64	44.83 ± 2.38
	40	0.81 ± 0.02	22.5 ± 7.51	42.15 ± 0.15
	60	0.97 ± 0.34	78.4 ± 31.2	38.95 ± 3.80
		0.90 ± 0.08	46.9 ± 20.0	41.98 ± 2.20

starting the crystalline transformation to recover the initial position. In addition, the transformation from austenite to martensite also requires external mechanical stress applied to the material, increasing the complexity of the recovery. In this case, the SE wire provides enough mechanical stress applied to the SME wire to recover the wire without adding more complexity to the system, and without this external stress the SME wire would barely recover the angular position. These recovery limitations constrain the application of the actuator into real-world scenarios, as the movement must be slow to have enough time to recover the original position, but the combination of passive recovery with external mechanical forces can further enhance the recovery and thus the actuator's performance.

4. Discussion

The hinge is able to follow different trajectories across different target angles and actuation times thanks to the integration of sensing and control into the SMA-actuator system. Table 5 presents the qualitative results of the test, separated in actuation time and angle setpoint analysis, to study how each of these reference parameters affects the outcome. For evaluating the performance of the heating phase, the metrics are the root mean square error between the target trajectory and the angle readings from the sensor, and the mean current per second applied to the wire to evaluate the thermal profile for each test. For the cooling phase, the table represents the percentage of recovered angle after letting the hinge cool down for two minutes. The first part of the table represents the mean and standard deviation for each metric and for each actuation time, meaning that the tests that have the same angle setpoint are combined. The second part maintains the same concept but in this case the angle setpoint is the variable that combines the tests.

Focusing on the heating results, the higher errors in the trajectory following appear in lower actuation times. This is coherent with the previous graphical representation in figure 9, where the inertia of the material at the beginning of the test is more noticeable. However, the angle setpoint does not appear to have any effect on the error, as for all of them the values are very similar and do not follow any pattern. In terms of energy, the higher frequency and setpoint signals require more current per second, as the heating must be faster and thus the current applied must be greater. However, in general, the system energy consumption stays under 100 mA per second, with a mean value across all the tests of approximately 50 mA per second, making the system energetically efficient when compared to other SMA-based actuation devices. In the cooling phase, the actuation time clearly impacts in the recovery, as lower values present higher recovery percentages across all angle setpoints, because the heating is faster and the system accumulates less heat. The target angle also influences the recovery, because lower angles require less heat to reach the reference value, and then the temperature is lower and the material recovers easier.

Overall, the MRSE is $0.90 \pm 0.08°$ for all tests, meaning that the hinge can follow the reference trajectory with an error of less than 1°, providing feasible results of the ability of the system to be used in applications where controlled movement is required. In addition, the standard deviation value highlights the repeatability of the results, ensuring consistent behavior in trajectory following. For the recovery, even though the target angle and actuation time affect the recovery, the mean value for all tests is $41.98 \pm 2.20\%$, meaning that the recovery is mainly affected by the actuator's torque and the properties of each SME-SE wire. This recovery value is the main limitation of the actuator, and it is closely related with the thermal nature of the SMA's transformation, as it needs time and external forces to recover its initial position.

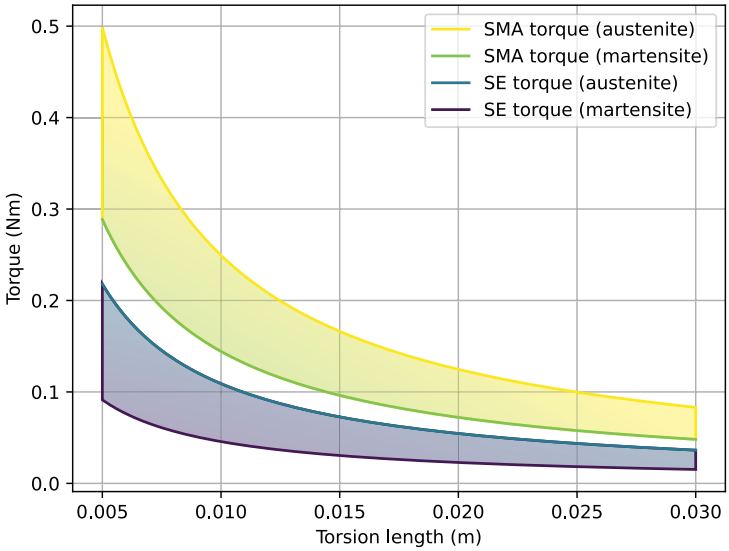

Figure 11. Actuator's torque evolution for varying torsion lengths, according to equation (9), for both the SME and the SE Nitinol wires used in the actuator. These curves allow the evaluation of the exerted torque by each of the wires and provide a tool for dimensioning the wires to obtain torque balance in the final actuator.

Following prior research [35] data, further torque balance in the SME-SE actuator can be done by combining the equations (1) and (2). The obtained equation (9) relates the produced torque (τ) when the actuator is deformed certain angle (θ) with the actuator's parameters, such as torsion length (L_T), wire diameter (D) and shear modulus ($G(\xi)$). The shear modulus of the wires is expressed as phase-fraction dependent weighted by the martensitic volume fraction ξ, which can be stress or temperature induced, according to equation (10), so the torque produced by each wire is bounded between fully austenite, $\xi = 0$, and fully martensite $\xi = 1$.

As the shear modulus is a material's property, the torque of the SME-SE wires is modified by varying the geometrical parameters: wire diameter which increases the torque, and torsion length which reduces the torque. Overall, the wires are available for purchasing in fixed diameters, so modifying the torsion length during the training in the ceramic oven is the best approach for obtaining the desired torque,

$$\tau(\theta) = \frac{\pi D^4 G(\xi)}{32 L_T}\theta \tag{9}$$

$$G(\xi) = (1-\xi)\, G_A + \xi\, G_M \quad ; \quad \xi \in [0,1] \tag{10}$$

This relationship provides a guideline for actuator design in terms of torque balance analysis. The necessary torque to deform the wire at a certain angle can be evaluated as a function of the actuator's geometric parameters variations. Even though this relationship does not consider the mechanical frictions produced in the hinge, and, the subsequent torque losses, studying these curves can ease the design process by giving a first good approximation of the actuator's forces. Assuming the angle is $\theta = 1$, then figure 11 represents the calculated torque range for the SME [36] and SE [38] wires as the torsion length increases.

These curves constitute a tool to assess the necessary torsion length for both wires to ensure that they are able to provide enough torque to deform the other wire and change its angular position, reaching the optimized combination of values and then maximizing the hinge's operating range. For instance, the SE wire must produce a torque lower than the E wire in austenite phase, so the hinge can close upon heating; but a torque higher than the SME wire in martensite phase to deform it back to its initial angle. Estimating the produced torque for each wire is not as straightforward, as these curves assume binary SMA states, either austenite or martensite, when in reality the transformation is more complex and produces a combination of states instead of a single state. Additional research to increase the actuator motion range includes more material's behavior analysis to optimize the SME-SE actuation forces and reach the best torque balance.

The torque balance greatly affects on the recovery of the SMA-based actuator. However, this partial recovery, although has great impact in the performance, is very well studied because it is very common when working with SMA-based actuators. One of the simplest solutions to overcome this problem is to use active cooling methods to quickly dissipate the actuator's heat and reduce its temperature,

as proposed in [40], where they use active cooling to improve the actuation bandwidth of a modular SMA actuator. Another common approach is to use antagonistic actuation, as in [41], where high-speed switching cycles are obtained through the decoupling of antagonistically arranged SMA wires, but in this case the complexity of the system scales as you double the actuation forces. This work shows the potential of SMA hinges as a very dense actuator to create modular and lightweight structures that can follow predefined movements. Further research is needed in areas such as materials engineering and systems design, to develop SMA-based actuators with increased range of movement and actuation time, as well as total recovery of its original position.

5. Conclusions

In this work, we presented a modular hinge actuator based on antagonistic SMA wires with integrated sensing and control, demonstrating reliable bending motion along predefined trajectories and applicability in reconfigurable morphing structures. The results highlight both the potential and the current limitations of SMA hinges: while actuation forces and controllability are promising, limited recovery remains a challenge for long-term and cyclic use.

The main contribution is the design and implementation of the combined SMA actuator and Hall effect sensor system that allows for movement tracking and control. This miniaturized design results in a compact hinge that can be combined and extended into more complex shape-morphing structures, where applications are often constrained in terms of adaptability, modularity, and compactness.

Another key contribution is the design guideline to apply torsional SMA actuators to these kind of morphing systems, where the geometric and dynamic analysis are crucial to understand the actuator behavior and constraints, specially in terms of torque balance and applied forces. Nevertheless, the hinge concept opens up new opportunities for modular and designer-friendly prototyping of morphing systems.

Future work should focus on extending the actuator toolkit with rotational elements, improving recovery through hybrid designs or active cooling, and exploring durability under real-world conditions. Additionally, the scalability of the system depends strongly on task-specific constraints, which requires developing high-level controllers and strategies to coordinate inter-hinge movements and improve energy efficiency.

Overall, the presented work establishes an initial validation of how sensing and control integration, when incorporated into smart material design paradigms, open opportunities to develop advanced shape-morphing devices and improve the tools available in design. We believe that these advances will bring SMA-based actuators closer to practical applications in robotics, adaptive interfaces, and interactive design, ultimately lowering the barriers for designers and engineers to use smart materials in shape-morphing systems.

Data availability statement

The data cannot be made publicly available upon publication because they are not available in a format that is sufficiently accessible or reusable by other researchers. The data that support the findings of this study are available upon reasonable request from the authors.

Acknowledgments

This collaboration is funded by the University Carlos III of Madrid.

Funding

This research was supported by an internal funding from Delft University of Technology (TU Delft). The project has been funded by Grant PID2023-149141OB-100, supported by

MICIU/AEI/10.13039/501100011033 and by the ERDF/EU.

Author contributions

Carmen Ballester 0000-0001-6098-8880

Conceptualization (equal), Data curation (lead), Formal analysis (lead), Investigation (equal), Methodology (equal), Software (lead), Validation (lead), Visualization (lead), Writing – original draft (lead)

Kaspar Jansen 0000-0002-2172-9824
Funding acquisition (lead), Investigation (equal), Methodology (equal), Project administration (equal), Supervision (equal), Writing – review & editing (equal)

Dorin Copaci 0000-0002-3070-0994
Funding acquisition (equal), Project administration (equal), Resources (equal), Writing – review & editing (equal)

Sepideh Ghodrat 0000-0002-4450-8178
Conceptualization (equal), Formal analysis (equal), Funding acquisition (equal), Investigation (equal), Methodology (equal), Project administration (equal), Resources (equal), Supervision (lead), Validation (equal), Writing – review & editing (lead)

References

[1] Bengisu M and Ferrara M 2018 *Materials That Move* (Springer)
[2] Figueiredo A, Modenesi P and Buono V 2009 Low-cycle fatigue life of superelastic NiTi wires *Int. J. Fatigue* **31** 751–8
[3] Kim M-S, Heo J-K, Rodrigue H, Lee H-T, Pane S, Han M-W and Ahn S-H 2023 Shape memory alloy (SMA) actuators: the role of material, form and scaling effects *Adv. Mater.* **35** 2208517
[4] Copaci D-S, Blanco D, Martin-Clemente A and Moreno L 2020 Flexible shape memory alloy actuators for soft robotics: modelling and control *Int. J. Adv. Robot. Syst.* **17** 1729881419886747
[5] Costanza G and Tata M E 2020 Shape memory alloys for aerospace, recent developments and new applications: a short review *Materials* **13** 1856
[6] Nair V S and Nachimuthu R 2022 The role of niti shape memory alloys in quality of life improvement through medical advancements: a comprehensive review *Proc. Inst. Mech. Eng. H* **236** 923–50
[7] Jani J M, Leary M and Subic A 2016 Designing shape memory alloy linear actuators: a review *J. Intell. Mater. Syst. Struct.* **28** 1699–718
[8] Stroud H and Hartl D 2020 Shape memory alloy torsional actuators: a review of applications, experimental investigations, modeling and design *Smart Mater. Struct.* **29** 113001
[9] Velvaluri P, Soor A, Plucinsky P, de Miranda R L, James R D and Quandt E 2021 Origami-inspired thin-film shape memory alloy devices *Sci. Rep.* **11** 10988
[10] Zhakypov Z and Paik J 2018 Design methodology for constructing multimaterial origami robots and machines *IEEE Trans. Robot.* **34** 151–65
[11] Benafan O, Moholt M R, Bass M, Mabe J H, Nicholson D E and Calkins F T 2019 Recent advancements in rotary shape memory alloy actuators for aeronautics *Shape Mem. Superelasticity* **5** 415–28
[12] Kim S-R, Lee D-Y, Koh J-S and Cho K-J 2016 Fast, compact and lightweight shape-shifting system composed of distributed self-folding origami modules *2016 IEEE Int. Conf. on Robotics and Automation (ICRA)* (IEEE) pp 4969–74
[13] Sheng J, Gandhi D, Gullapalli R, Simard J M and Desai J P 2017 Development of a meso-scale SMA-based torsion actuator for image-guided procedures *IEEE Trans. Robot.* **33** 240–8
[14] Wang W, Rodrigue H and Ahn S-H 2016 Deployable soft composite structures *Sci. Rep.* **6** 20869
[15] Chen X, Bumke L, Quandt E and Kohl M 2023 Bistable actuation based on antagonistic buckling SMA beams *Actuators* **12** 422
[16] Bedenik G, Morales A, Pieris S, da Silva B, Kurelek J W, Greeff M and Robertson M 2025 Bistable SMA-driven engine for pulse-jet locomotion in soft aquatic robots *2025 IEEE 8th Int. Conf. on Soft Robotics (RoboSoft)* (*Lausanne, Switzerland, 22–26 April 2025*) (IEEE) pp 1–8
[17] Banu Sundareswari M, Then Mozhi G and Dhanalakshmi K 2021 Angular control of differential shape-memory alloy spring actuator for underactuated dynamic system *J. Vib. Control* **28** 2829–43
[18] Xu Y, Zhuo J, Fan M, Li X, Cao X, Ruan D, Cao H, Zhou F, Wong T-W and Li T 2024 A bioinspired shape memory alloy based soft robotic system for deep-sea exploration *Adv. Intell. Syst.* **6** 2300699
[19] Patterson Z J, Sabelhaus A P and Majidi C 2022 Robust control of a multi-axis shape memory alloy-driven soft manipulator *IEEE Robot. Autom. Lett.* **7** 2210–7
[20] Shi E, Zhong X, Wang T, Li X, Bu C and Zhao X 2024 Adaptive control for shape memory alloy actuated systems with applications to human-robot interaction *Front. Neurosci.* **18** 1337580
[21] Wertz A, Sabelhaus A P and Majidi C 2022 Trajectory optimization for thermally-actuated soft planar robot limbs *2022 IEEE 5th Int. Conf. on Soft Robotics (RoboSoft)* (IEEE) pp 439–46
[22] Mersch J, Keshtkar N, Grellmann H, Cuaran C A G, Bruns M, Nocke A, Cherif C, Robenack K and Gerlach G 2022 Integrated temperature and position sensors in a shape-memory driven soft actuator for closed-loop control *Materials* **15** 520
[23] Rodino S, Caroleo G, Sgambitterra E, Bruno F, Muzzupappa M and Maletta C 2023 A multiphysics dynamic model for shape memory alloy actuators *Sens. Actuators A* **362** 114602
[24] Cortez R, Sandoval-Chileno M A, Lozada-Castillo N and Luviano-Juarez A 2024 Snake robot with motion based on shape memory alloy spring-shaped actuators *Biomimetics* **9** 180
[25] Motzki P, Khelfa F, Zimmer L, Schmidt M and Seelecke S 2019 Design and validation of a reconfigurable robotic end-effector based on shape memory alloys *IEEE/ASME Trans. Mechatronics* **24** 293–303
[26] Kim H, Everitt A, Tejada C, Zhong M and Ashbrook D 2021 Morpheesplug: a toolkit for prototyping shape-changing interfaces *Proc. 2021 CHI Conf. on Human Factors in Computing Systems, CHI'21, ACM* pp 1–13
[27] Li Y, Zhao Y, Chi Y, Hong Y and Yin J 2021 Shape-morphing materials and structures for energy-efficient building envelopes *Mater. Today Energy* **22** 100874
[28] Zhang Y, Yang J, Liu M and Vella D 2022 Shape-morphing structures based on perforated kirigami *Extreme Mech. Lett.* **56** 101857
[29] Liu Q, Ghodrat S and Jansen K M B 2024 Mimosa: modular self-folding hinges kit for creating shape-changing objects *Proc. 18th Int. Conf. on Tangible, Embedded and Embodied Interaction, TEI'24, ACM* pp 1–13

[30] An N, Li M and Zhou J 2020 Modeling SMA-enabled soft deployable structures for kirigami/origami reflectors *Int. J. Mech. Sci.* **180** 105753
[31] Saeedi A, Kwon H, Soni P, Dillenburger B and Shahverdi M 2024 Design and multiphysical modeling of SMA-driven bi-stable structures with efficient energy consumption *Eng. Struct.* **314** 118367
[32] Zheng K, Gao E, Tian B, Liang J, Liu Q, Xue E, Shao Q and Wu W 2022 Modularized paper actuator based on shape memory alloy, printed heater and origami *Adv. Intell. Syst.* **4** 2200194
[33] Jin H, Dong E, Alici G, Mao S, Min X, Liu C, Low K H and Yang J 2016 A starfish robot based on soft and smart modular structure (SMS) actuated by SMA wires *Bioinsp. Biomim.* **11** 056012
[34] Xiao J, Wang M Y and Chen C 2024 A novel shape memory alloy modular robot with spatially stable structure *Adv. Intell. Syst.* **6** 2400091
[35] Liu Q, Ghodrat S and Jansen K M 2024 Design and modelling of a reversible shape memory alloy torsion hinge actuator *Mater. Des.* **237** 112590
[36] Nitinol shape memory alloy wire, d = 1 mm, af = 45-50 °c 2025 (available at: https://shop.nanografi.com/shape-memory-materials/nitinol-shape-memory-alloy-wire-diameter-1-mm-af-45-50-c/) (Accessed 24 August 2025)
[37] Nitinol superelastic wire ASTM f2063 all sizes - nexmetal corporation2025 (available at: https://nexmetal.com/products/nitinol-superelastic-wire?variant = 21956546436) (Accessed 12 December 2025)
[38] Nitinol, super-elastisch draad d = 0,83 mm 2025 (available at: www.titaniumshop.nl/nl/nitinol/nitinol-super-elastisch-draad-d-0-83mm-per-20-centimeter/a-4968-80) (Accessed 24 August 2025)
[39] Tle493d-a2b6 low power 3d hall sensor with i2c interface - datasheet (ver. 1.3, 2019-04-09) 2019 (available at: https://nl.mouser.com/datasheet/2/196/Infineon-TLE493D-A2B6-DataSheet-v01_30-EN-1732243.pdf) (Accessed 24 August 2025)
[40] Ding Q, Chen J, Yan W, Yan K, Kyme A and Cheng S S 2022 A high-performance modular SMA actuator with fast heating and active cooling for medical robotics *IEEE/ASME Trans. Mechatronics* **27** 5902–13
[41] Britz R, Rizzello G and Motzki P 2022 High-speed antagonistic shape memory actuator for high ambient temperatures *Adv. Eng. Mater.* **24** 2200205